2016

Super-Maxwellian Helium Evaporation from Pure and Salty Water

Christine Hahn
University of Wisconsin-Madison

Zachary R. Kann
University of Wisconsin-Madison

Jennifer Faust
The College of Wooster, jfaust@wooster.edu

J. L. Skinner
University of Wisconsin-Madison

Gilbert M. Nathanson
University of Wisconsin-Madison

Super-Maxwellian helium evaporation from pure and salty water

Christine Hahn, Zachary R. Kann, Jennifer A. Faust, J. L. Skinner,[a)]
and Gilbert M. Nathanson[a)]
Department of Chemistry, University of Wisconsin-Madison, 1101 University Avenue, Madison, Wisconsin 53706, USA

(Received 30 November 2015; accepted 5 January 2016; published online 27 January 2016)

Helium atoms evaporate from pure water and salty solutions in super-Maxwellian speed distributions, as observed experimentally and modeled theoretically. The experiments are performed by monitoring the velocities of dissolved He atoms that evaporate from microjets of pure water at 252 K and 4–8.5 molal LiCl and LiBr at 232–252 K. The average He atom energies exceed the flux-weighted Maxwell-Boltzmann average of $2RT$ by 30% for pure water and 70% for 8.5m LiBr. Classical molecular dynamics simulations closely reproduce the observed speed distributions and provide microscopic insight into the forces that eject the He atoms from solution. Comparisons of the density profile and He kinetic energies across the water-vacuum interface indicate that the He atoms are accelerated by He–water collisions within the top 1-2 layers of the liquid. We also find that the average He atom kinetic energy scales with the free energy of solvation of this sparingly soluble gas. This free-energy difference reflects the steeply decreasing potential of mean force on the He atoms in the interfacial region, whose gradient is the repulsive force that tends to expel the atoms. The accompanying sharp decrease in water density suppresses the He–water collisions that would otherwise maintain a Maxwell-Boltzmann distribution, allowing the He atom to escape at high energies. Helium is especially affected by this reduction in collisions because its weak interactions make energy transfer inefficient. [http://dx.doi.org/10.1063/1.4940144]

I. INTRODUCTION

Molecules residing in the gas or liquid phases collide with each other through energy-exchanging events that enforce a Maxwell-Boltzmann (MB) distribution of speeds at equilibrium.[1,2] This criterion also holds for molecules traversing the interface between equilibrium gas and liquid phases.[3,4] Trajectories starting in the gas phase consist of impulsive scattering from the surface, trapping and immediate desorption, and collisions that lead to entry into the liquid.[5] The initial energy distribution for each channel may individually deviate from a MB distribution, but must sum together to be Maxwellian. In particular, higher collision energies often favor impulsive scattering while lower energies lead to trapping.[3,6,7] The energy distribution for solute entry (dissolution) may also deviate from a MB distribution; because dissolution and evaporation are microscopically reversed processes, the evaporating solute must then desorb with non-Maxwellian kinetic energies as well.[3,6,8–11]

We explore in this study the evaporation of helium atoms from water by isolating this pathway from all other scattering channels. This isolation can be achieved experimentally by monitoring solute evaporation in vacuum, where impingement onto the surface is suppressed, and by computer simulations of the evaporation process itself. Among solute species, helium atoms appear to be special because of their weak attraction to the solvent and shallow adsorption well. We find that this sparingly soluble gas evaporates in strongly super-Maxwellian distributions that depend on temperature and solvent composition. As shown below, the kinetic energies of evaporating He atoms from pure and salty water scale with the free energy of solvation, whose magnitude reflects the repulsive forces that eject the He atom from the interfacial region into vacuum.

Non-Maxwellian evaporation from solid surfaces has a rich history. High-energy desorption has been observed for the products of exothermic chemical reactions, such as H(ads) + H(ads) → H_2(gas) and CO(ads) + O(ads) → CO_2(gas).[8,10,12–14] In these cases, much of the reaction exothermicity is channeled into the translational and internal energies of the gas-phase products. In contrast, non-reactive desorption may lead to sub-Maxwellian velocity distributions, as observed for Ar atoms desorbing from tungsten and platinum.[3,6] This low-energy evaporation may be understood by invoking detailed balance: lower-energy Ar atoms impinging on a surface preferentially adsorb because they have less energy to dissipate, and so in reverse, only lower-energy Ar atoms desorb. Kinematically, adsorbates with much lower mass than the substrate do not exchange energy efficiently: lower desorption energies might then be expected if Ar atoms having just enough energy to climb out of the adsorption well do not undergo sufficient collisions to regain the full energy of translation as they exit.[9]

The first translational energy measurements of evaporating species from pure water were carried out by Faubel and co-workers using narrow-diameter microjets in vacuum.[15] They measured a Maxwellian speed distribution

[a)]Authors to whom correspondence should be addressed. Electronic addresses: skinner@chem.wisc.edu and nathanson@chem.wisc.edu

for evaporating water molecules but also observed super-Maxwellian evaporation of acetic acid dimer from a dilute aqueous solution.[16] This high-energy departure was attributed to the formation of the hydrophobic $(CH_3COOH)_2$ pair from the hydrogen-bonding monomers. The dimer is then ejected as the surface flattens to minimize its surface free energy.

We have previously observed super-Maxwellian He evaporation from microjets of pure and mixed hydrocarbons and ethylene glycol.[17,18] The evaporation of He from liquid dodecane was modeled through molecular dynamics simulations by Williams and Koehler; they found that He atoms were preferentially accelerated to higher energies when they emerged from craters at the surface that filled in and pushed the He atom outward into the vacuum.[19] Nelson and Benjamin have also simulated high-energy He evaporation from ethylene glycol.[20] Intriguingly, the unusual behavior of interfacial He atoms was inferred earlier by Phillips through measurements of the Onsager heat of transport.[21] Because of their weak attractions to solvent molecules and their small size, He atoms evaporate in the most non-Maxwellian distribution of all gases. Neon atoms also evaporate at slightly higher energies, while H_2 evaporates in a sub-Maxwellian distribution.[22] Other more polarizable gases, such as Ar, O_2, N_2, H_2O, CO_2, HCl, and HNO_3 are found to evaporate experimentally[18,23,24] and theoretically[25,26] in Maxwellian distributions, but distinct deviations appear in simulations of angle-resolved Ar evaporation.[27,28]

In this study, we describe microjet experiments and classical molecular dynamics simulations to explore He evaporation from pure water at 252 K and salty solutions containing 4, 8, and 8.5 molal LiBr and 4 and 8 molal LiCl at 232–252 K. The experiments demonstrate that He atoms exit at high energies from all solutions and reach 70% higher average energies than the expected flux-weighted value of $2RT_{liq}$ for He evaporation from 8.5m LiBr at 235 K. Molecular dynamics simulations closely reproduce the speed distributions and capture trends in temperature and salt composition. In particular, the computed potential of mean force provides guidance in evaluating the forces on the He atom as the water structure relaxes upon expelling the solute atom. The correlation between the He kinetic energy and solvation free energy appears to apply not only to pure and salty water but also to dodecane and ethylene glycol as well.

II. EXPERIMENTAL AND THEORETICAL PROCEDURES

A. Experimental methods

The microjet solutions are prepared by dissolving polycrystalline LiBr and LiCl (Sigma-Aldrich; LiCl, ACS reagent, ≥99%; LiBr, ReagentPlus, ≥99%) in Millipore water and filtering to trap insoluble residues. Before each experiment, the solutions are degassed under vacuum to ~20 Torr to remove dissolved air. Pure He or Ar gas is then dissolved into the solution by vigorously shaking the liquid in a 2 L steel reservoir under 5-18 atm of gas.

Figure 1(a) depicts the microjet assembly.[18] Pure and salty water microjets are created by forcing the pressurized

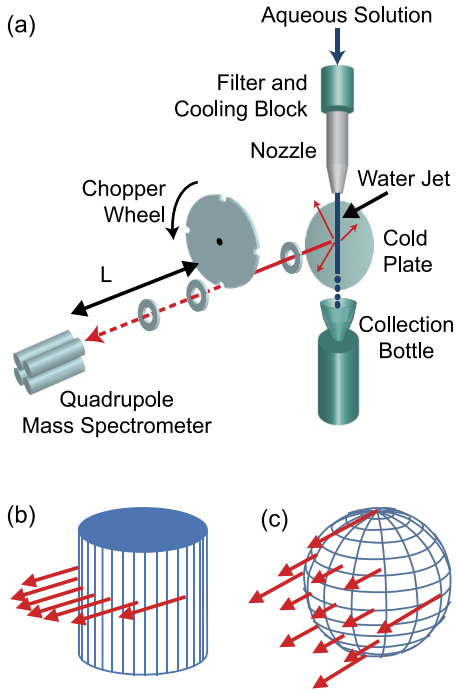

FIG. 1. (a) Liquid microjet apparatus. Helium atoms evaporate in all directions from the water microjet, which may be in cylinder or droplet form. Atoms traveling toward the mass spectrometer are chopped into pulses and recorded as a time-of-flight (TOF) spectrum. Evaporation measured along this one direction sums over many exit angles from (b) a cylindrical jet and (c) a spherical droplet.

solution through a tapered glass nozzle. The radii of the glass nozzles are determined from microscope images and range from 5 μm for pure water to 17 μm for the 8m solutions, as listed in Table I. The actual jet radii are probably less than the measured openings.[29] Any remaining particulates are removed by two additional filters before the solution enters the nozzle. In order to avoid freezing, the pressure of the backing gas is gradually increased to its final value as the vacuum chamber is evacuated and the solutions are cooled to the target temperature by a copper block situated just before the nozzle exit. After passing through the chamber, the solution is collected in vacuum in a 2 L glass bottle cooled by an ethanol/dry ice bath. Liquid nitrogen-cooled panels freeze out water evaporating from the jet and lower the background pressure to 10^{-5} Torr when the jet is running. Two 2000 L s^{-1} diffusion pumps remove He and other non-condensable gases.

He and Ar atoms evaporating from the cylindrical jet (Fig. 1(b)) or droplets (Fig. 1(c)) are monitored by a doubly differentially pumped quadrupole mass spectrometer, which views a 1.0 mm or 5.6 mm circular region (depending on collimating aperture) starting at a distance of 1-3 mm below the nozzle tip. The continuously evaporating gas is chopped into 48 μs pulses, and their arrival times are recorded over the L = 19.6 cm flight path in a time-of-flight (TOF) spectrum. A trial function $N_{fit}(t)$ is then convoluted with the finite gas pulse to account for the broadening created by the chopper wheel. This trial function is a sum of 3–4 terms of the form $t^{-4}A_i \exp(-B_i[(L/t) - C_i]^2)$, where the variables A_i, B_i, and C_i are adjusted to obtain the best fit to the TOF spectrum.[18] In addition, a small background arising from the jet at m/z = 4

TABLE I. Microjet parameters.[a]

Liquid	T_{liq} (K)	r_{jet} (μm)	u_{jet}[b] (m s^{-1})	$L_{breakup}$ (mm)	P_{vap}[c] (Torr)	λ (μm)	N_{coll}
Water	252	5	21	<1	0.9	400	0.07
4*m* LiCl	252	10	13	1.3	0.7	500	0.09
8*m* LiCl	248	17.5	14	3.5	0.3	1000	0.06
8*m* LiCl[d]	232	17.5	16	5.3	0.07	5000	0.02
4*m* LiBr	246	10	21	2.0	0.4	800	0.05
8*m* LiBr	259	10	16	1.8	0.8	500	0.1
8*m* LiBr[d]	237	17.5	25	7.5	0.1	3000	0.02
8.5*m* LiBr[d]	235	17.5	20	7.0	0.1	3000	0.04

[a]T_{liq} is the liquid temperature in the observation region from argon thermometry, r_{jet} is the nozzle radius, u_{jet} is the jet speed, $L_{breakup}$ is the cylinder to droplet breakup length, P_{vap} is the liquid vapor pressure, and λ and N_{coll} are the He–H_2O mean free path and collision probability for a collision cross section σ of 15 Å^2. See Eqs. (2) and (3) of Ref. 18 for calculations of $L_{breakup}$ and N_{coll}. (N_{coll} was conservatively estimated using the cylinder equation in all cases by setting the jet length to 8 mm and the collision distance R to 1 mm for the 1 mm viewing region and 50 mm for the 5.6 mm viewing region.) Except where noted, all measurements were made using a 1.0 mm dia viewing region of the jet.

[b]Calculated from the flow rate and jet area using r_{jet} as the jet radius.

[c]Based on Refs. 75 and 76 (LiBr) and Refs. 54 and 77 (LiCl).

[d]5.6 mm dia viewing regions were used for 1 of 5 measurements of 8*m* LiCl/232 K, 1 of 3 measurements for 8.5*m* LiBr/235 K, and the single measurement of 8.5*m* LiBr/235 K.

is subtracted from each spectrum (consistent with D_2^+ from D_2O).

The liquid jet begins as a cylinder and then breaks up into droplets, as pictured in Fig. 1(a).[29,30] Pure water and the warmer salt solutions form jets that have short breakup lengths (listed in Table I) and appear as droplets in the observation region, while the colder and saltier solutions appear as cylindrical jets. Panels (b) and (c) illustrate that only He atoms evaporating along the line of sight of the mass spectrometer are detected, but this narrow-angle detection still leads to significant angular averaging because of the curvature of the cylinder and droplets. The He flux from the droplets is roughly half the flux from the cylinder.

B. Theoretical methods

Surface simulations were conducted in the NVT ensemble with the temperature maintained by a Nosé–Hoover thermostat[31] with a time constant of 0.1 ps. Periodic boundary conditions were employed using the particle-mesh Ewald (PME) method to calculate long-range electrostatics. Lennard-Jones and short-range electrostatic interactions were cut off at 1.0 nm. A 1.0 fs time step was employed, with snapshots saved every 10–100 time steps, depending on temperature. The GROMACS 4.5.5 software package[32,33] was used for all simulations.

While the E3B water model[34] was used for simulations of pure water, we chose the TIP4P/2005[35] model for salty solutions because E3B has only been tested with scaled-charge ions,[36] which may not be readily usable in interfacial systems. Ion parameters were taken from Mao and Pappu,[37] and the spherical helium-water interaction potential was taken from Bickes *et al.*[38–40] All other interactions were determined according to Lorentz-Berthelot mixing rules.[41–43]

Slab geometries were created for the surface simulations by first equilibrating the aqueous system without helium atoms for 500 ps in a 3 nm cubic simulation box. After initial equilibration, the z dimension of the box was extended to a length of 9 nm, creating two surfaces. The slabs were then equilibrated for another 1.0 ns before adding any helium atoms. Ten water molecules were replaced with helium atoms, with the sole requirement being that the chosen molecules be in the aqueous slab at least 1.0 nm from either of the slab's surfaces. The simulations were then run for 0.5-3.0 ns, depending on the temperature and ion concentration. This time was chosen to allow at least 75% of the He atoms to evaporate in nearly every simulation. The distribution of He atom velocities was determined by recording each atom's velocity the first time it crossed a plane in the vapor region 2.0 nm from either surface of the slab. This method, including the equilibration phases, was repeated 500 times for a total of 5000 potential helium evaporation events at each temperature and ion concentration.

The average energy $\langle E_{evap} \rangle$ and energy distributions $P_{He}(E)$ of evaporating He atoms are then computed from the simulations of He atoms exiting from the flat surface. The average evaporation energy of He atoms traveling in a single direction from a spherical droplet (Fig. 1(c)) is geometrically equivalent to an average over all trajectories from a flat surface. To obtain the analogous kinetic energy of He atoms evaporating in a single direction from a cylindrical jet (Fig. 1(b)), the flat-surface kinetic energies are weighted by $(\sin\theta)^{-1}$, where θ is the angle with respect to the local surface normal. We find that the cylinder evaporation energies are at most 6% greater than the droplet values. To provide consistent comparisons among the simulations, we use the droplet evaporation energies in all instances in the figures and text.

The potential of mean force calculations were conducted in the same slab geometry, but with only a single He atom present in the aqueous slab. The weighted histogram analysis method (WHAM), as implemented in the g_wham program,[44] was used to calculate the potential of mean force (PMF) from a series of 10 ns umbrella-sampling simulations. The biasing potential had a force constant of 1000 kJ mol^{-1} nm^{-1}, and the spacing between adjacent sampling windows was 0.025 nm.

Solvation free energies, ΔG^o_{solv}, were calculated using the Bennett acceptance ratio method[45] with 21 equally spaced λ

values. These simulations were conducted using cubic boxes in the NPT ensemble at 1 atm with the pressure maintained by a Parrinello-Rahman barostat[46] with a time constant of 1.0 ps; all other simulation parameters remained the same as in the above surface simulations. The simulations were equilibrated for 500 ps at each λ value followed by a 500 ps production run, during which time snapshots were saved every 100 fs. To avoid any aberrations due to finite-size effects, three box sizes were used: 2.5 nm, 3.2 nm, and 4.0 nm. The free energy was then graphed against (moles of water)$^{-1}$, with the intercept corresponding to the ΔG^{o}_{solv} values reported here.

III. LIQUID PROPERTIES AND MICROJET PARAMETERS

A. Liquid composition, helium solubility, and jet temperature

Table I lists selected properties of the aqueous microjets under our experimental conditions. The molal salt concentrations range from pure water at 252 K to 8*m* LiCl and 8.5*m* LiBr at temperatures from 232 to 252 K. Lithium salts were chosen because of their substantial solubility and freezing-point depressions,[47] which allow access to the 0.07–0.9 Torr vapor pressures listed in the table. In particular, LiCl and LiBr lower the 273 K freezing point of pure water to ~250 K (4*m* salt) and ~210 K (8*m* salt). These salty solutions are therefore within or close to the liquid region, while pure water at ~252 K is supercooled. The 4*m* (~4M) and 8*m* (~7M) solutions correspond to 14 and 7 water molecules per ion pair, respectively. Experiments and simulations indicate that 4–5 water molecules are tightly bound to Li^+ and 4–9 are more loosely bound to Cl^- and Br^-.[48,49] Even after accounting for shared solvation shells and ion pairing, these numbers imply that nearly every water molecule interacts directly with an ion in the 8*m* solutions.[50–52] The addition of LiCl and LiBr to water also increases the surface tensions[53–55] and viscosities[56] of the solutions, which rise as well when the temperature is lowered. For the solutions in Table I, the surface tensions and viscosities range from ~78 mN m^{-1} and ~5 mPa s for pure water at 252 K[57] to ~95 mN m^{-1} and ~30 mPa s for 8*m* LiCl at 232 K. LiBr solutions change in similar ways but with smaller increments.

Helium has the lowest polarizability among all gases (0.2 Å^3) and is the least soluble in water. Our calculations of the He free energy of solvation, $\Delta G^{o}_{solv} = -RT \ln(n(\mathrm{He})_{water}/n(\mathrm{He})_{gas})$, are plotted in Fig. 2 for pure water and 8.6*m* LiBr from 235 to 340 K, along with measured values of He in pure water.[58] The simulated and experimental free energies for pure water agree well, in all cases differing by less than 2 kJ mol^{-1}. At 255 K, the computed free energy of He in pure water is +9.7 kJ mol^{-1}, corresponding to a density ratio of $n(\mathrm{He})_{water}/n(\mathrm{He})_{gas} \approx 1/100$.[59] The He solubility is predicted to drop by roughly half in 8.6*m* LiBr, and ΔG^{o}_{solv} increases by 1.4 kJ mol^{-1}.[60] No calculations were performed for LiCl, but comparisons of He solubility in NaCl and NaBr solutions show little difference.[60] Helium is typically less soluble in alkali halide solutions than in pure water, in part because ion-water bonding ties up water molecules and reduces the number of sites for He solvation.[60–63] In all cases in Fig. 2, the free energies are positive and generally increase with temperature. These free energies are entropic in origin, as He dissolution is exothermic. In particular, $\Delta E^{o}_{solv} (= \Delta H^{o}_{solv} - RT_{liq})$ is approximately −2 kJ mol^{-1} for He in pure water near 250 K.[58] The adsorption energy of He at the surface of water is likely to be even smaller and close to −1/2 kJ mol^{-1}.[64]

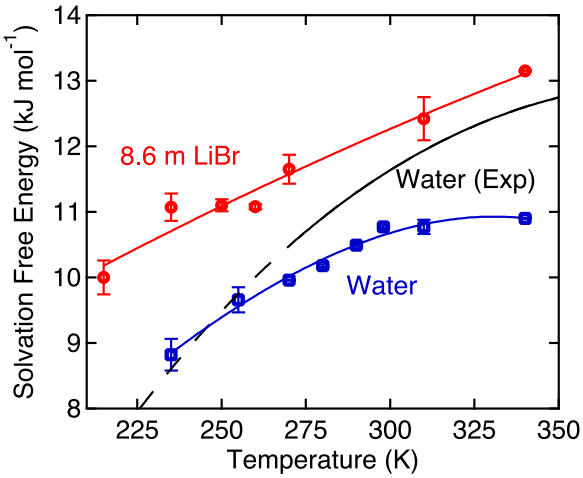

FIG. 2. Simulated values of ΔG^{o}_{solv} for helium in 8.6*m* LiBr solution (red circles) and pure water (blue squares) as a function of temperature. The red and blue lines are quadratic fits to the simulations. Experimental data (black line) for pure water are reproduced from Ref. 58. The dashed line is an extrapolation to the supercooled region.

B. Gas-vapor collisions and argon thermometry

The jet radius and liquid temperature T_{liq} (which sets the water vapor pressure) are chosen in part to minimize the number of collisions N_{coll} between the evaporating He atom and water molecules in the vapor cloud surrounding the cylindrical jet or droplet. These collisions must be suppressed because they alter the velocities of the evaporating solute species, often leading to an artificial narrowing of the TOF spectra.[16,18] Expressions derived by Faubel[29] and Sadtchenko[65] indicate that r_{jet} and T_{liq} should be chosen such that r_{jet} is substantially smaller than the He–H_2O mean free path λ_o (listed in Table I). λ_o is calculated from $(\sigma n_o/2)^{-1}$ where $n_o/2$ is the equilibrium water vapor density corresponding to the evaporation flux, and $\sigma \approx 15$ Å^2 is the He–H_2O cross section.[18] The values of N_{coll} in Table I range between 0.02 and 0.1. In practice, we vary r_{jet} and T_{liq} until the evaporation of dissolved argon atoms, which are larger and more polarizable than He atoms, follows a nearly Maxwellian velocity distribution. This Maxwellian Ar evaporation is an indicator of a collision-free environment surrounding the cylinder or droplet, as we found previously for Ar evaporation from low-vapor pressure liquids (such as squalane) that are not surrounded by a gas cloud.[17,18] One advantage of this argon criterion is that it provides a measurement of the temperature of the jet itself, as described below.

Each liquid jet cools by evaporation as it travels through the vacuum chamber, reducing the temperature of the liquid in the observation region.[29,30,66] To determine the actual

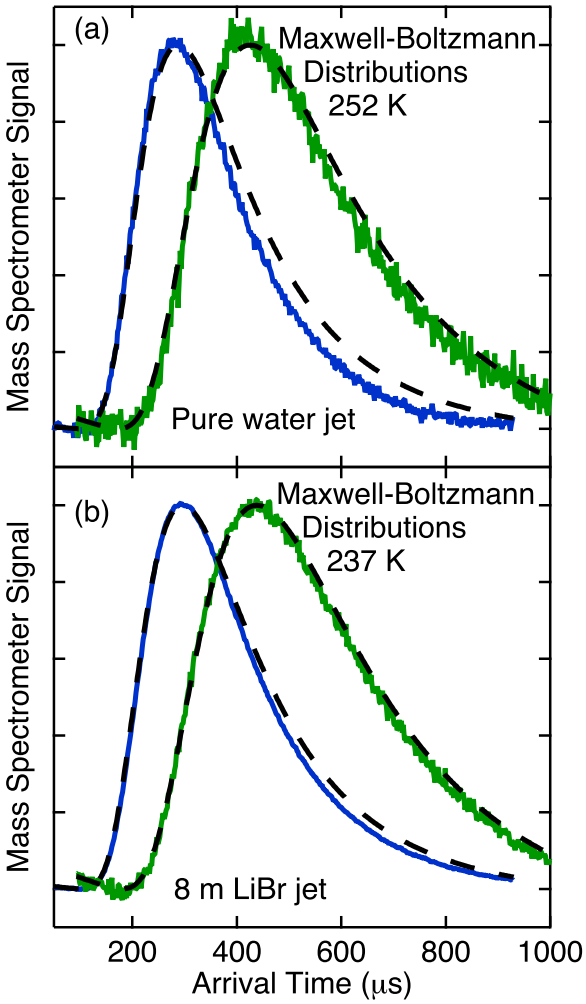

FIG. 3. TOF spectra of water (blue) and dissolved argon (green) evaporating from (a) pure water and (b) 8*m* LiBr/H_2O. The estimated liquid temperatures are (a) 252 K and (b) 237 K, based on Maxwell-Boltzmann fits (black dashed lines) to the Ar spectra.

temperature of the jet when it is viewed by the mass spectrometer, we fit the near-Maxwellian Ar evaporation spectrum to a single temperature, which is identified as T_{liq}. Fig. 3 illustrates this "argon thermometer" for a 5 μm radius jet of pure water pre-cooled in the glass nozzle to an initial temperature of ~280 K and for a 17.5 μm radius jet of 8*m* LiBr pre-cooled to ~237 K. In each panel, the evaporation distribution of water is slightly narrowed because of water–water collisions in the vapor cloud. Ar atoms evaporate in distributions that are more Maxwellian because of the smaller cross section for Ar–H_2O collisions. We fit the leading edge of the Ar spectra and determine jet temperatures of T_{liq} = 252 K for pure water (18 K cooling) and 237 K for LiBr/H_2O (no measurable cooling), with an estimated fitting uncertainty of ±3 K.

IV. SUPER-MAXWELLIAN HELIUM EVAPORATION

Figure 4(a) shows the TOF spectrum of He evaporating from pure water at 252 K in comparison with a He MB distribution. In contrast to Fig. 3, the He atoms arrive at significantly earlier times than predicted, implying higher

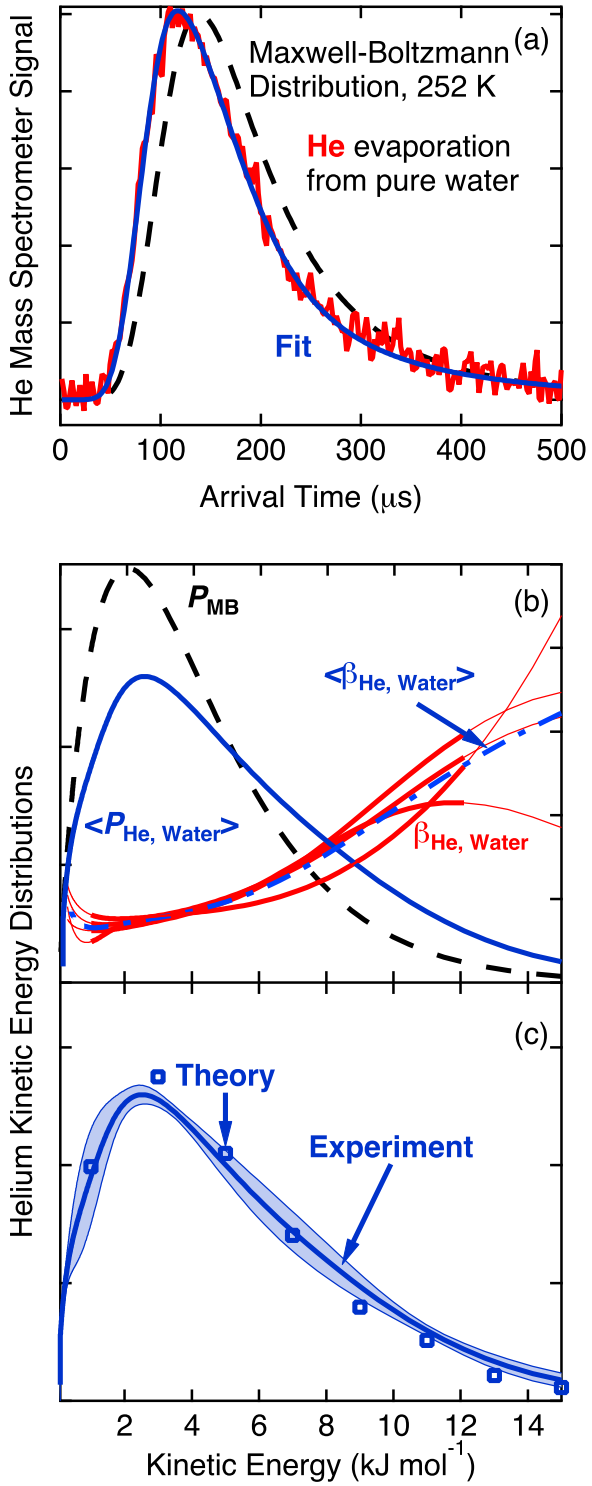

FIG. 4. (a) TOF spectrum of He atoms evaporating from pure water (red) with best fit (blue line) and Maxwell-Boltzmann (MB) distribution at 252 K (dashed black line). (b) He atom kinetic energy distributions: $\langle P_{He}\rangle$ (solid blue line) is the average of four measurements and P_{MB} (dashed black line) is the MB distribution at 252 K. Relative evaporation probability $\beta_{He}(E) = P_{He}(E)/P_{MB}(E)$: $\langle\beta_{He}\rangle$ (blue dash-dot line) is the average of four individual β_{He} (red lines) (c) Simulated (open squares) and experimental (blue line) $P(E)$ distributions. The shaded region reflects a 90% confidence interval.

velocities and kinetic energies. The best fit to the data, $N_{fit}(t)$, is depicted as the blue line.

The He kinetic energy distribution is derived from the TOF spectrum through the relation $P_{He}(E) = CN_{fit}(t)t^2$.[67]

In this expression, $P_{He}(E)$ is the relative flux distribution (relative evaporation probability) for He atoms leaving the jet with translational energy $E = {}^1/_2 m_{He}(L/t)^2$, normalized to unit area by the prefactor C. Figure 4(b) compares this flux distribution to its Maxwell-Boltzmann analog, given by $P_{MB}(E) = E/(RT_{liq})^2 e^{-E/RT_{liq}}$, whose average flux-weighted energy is $\langle E_{MB}\rangle = 2RT_{liq}$. The measured He energy distribution $\langle P_{He}(E)\rangle$ is averaged over four separate measurements. It is shifted to higher energies than $P_{MB}(E)$ and is characterized by an average energy of $(1.32 \pm 0.06) \times 2RT_{liq}$, or 32% greater than predicted by a MB distribution at 252 K. We note that all reported uncertainties in the multipliers of $2RT_{liq}$ contain three contributions: (a) 90% confidence interval using a single standard deviation calculated from 15 measurements with multiple trials, as listed in Table II; (b) a fitting uncertainty in $P_{He}(E)$ of $\pm 0.01 \times 2RT_{liq}$; and (c) a temperature uncertainty in T_{liq} of ±3 K.

Deviations from Maxwellian behavior in Fig. 4(b) can be gauged visually by graphing the ratio of normalized fluxes, $\beta_{He}(E) = P_{He}(E)/P_{MB}(E)$.[3,18] The dashed-dotted blue curve is the measured He evaporation probability relative to a MB distribution and would be a flat line if $P_{He}(E)$ (solid blue curve) and $P_{MB}(E)$ (dashed black curve) had the same shape. The rising $\beta_{He}(E)$ curve indicates that He atoms preferentially evaporate at higher energies with respect to a MB distribution. Because we measure only relative He fluxes, $P_{He}(E)$ and $P_{MB}(E)$ are each area-normalized, and only ratios of $\beta_{He}(E)$ are meaningful. As an example, the blue dashed-dotted curve in panel (b) shows that the ratio β_{He} (12 kJ mol^{-1})/β_{He} (2 kJ mol^{-1}) is approximately 4:1 instead of 1:1 for a MB distribution. This substantial deviation implies that the relative flux of He atoms in a MB distribution of P_{MB} (12 kJ mol^{-1})/P_{MB}(2kJ mol^{-1}) = 1:20 increases to 1:5 for He evaporating from pure water at 252 K.

The blue dashed-dotted curve for $\beta_{He}(E)$ in Fig. 4(b) represents an average over four measurements, whose individual values are shown by the red lines. Deviations are largest at high energies, where evaporation is weak, and are indicated by thin lines. There is also a small rise in $\beta_{He}(E)$ below 1 kJ mol^{-1}, but we are uncertain if this is real—it is also seen in simulations of He evaporation from dodecane.[19] Finally, Fig. 4(c) displays the simulated energies (open squares) at 255 K, averaged over 5000 trajectories, which match the measured energy distribution remarkably well. The slight underestimate at high energies leads to a smaller average energy of $(1.18 \pm 0.02) \times 2RT_{liq}$, in comparison with the experimental value of 1.32 ± 0.06 for He evaporation from pure water. These two values differ by only 0.6 ± 0.3 kJ mol^{-1}.

Figure 5 shows the analogous TOF spectra, energy distributions, and relative evaporation probabilities for He atoms evaporating from 8*m* LiBr at 237 K (3 measurements) and 8*m* LiCl at 232 K (5 measurements). The average He evaporation energies are even higher for these salty solutions than for pure water, reaching $(1.60 \pm 0.07) \times 2RT_{liq}$ for LiBr and $(1.64 \pm 0.08) \times 2RT_{liq}$ for LiCl. The similarities in these average energies and the energy distributions in panel (b) imply that the forces that expel the He atoms from the solutions do not depend on differences in the interfacial Cl^- and Br^- ions. There are small deviations in $\beta_{He}(E)$ for $E > 9$ kJ mol^{-1}, which likely lie within the fitting uncertainties. For these curves, the average value of β_{He}(12 kJ mol^{-1})/β_{He}(2 kJ mol^{-1}) = 9 is over twice the ratio for pure water at 252 K. Panel (c) again shows that the simulations match the experimental He kinetic energy distribution remarkably well for 8.5*m* LiBr at 235 K (experiment) and 8.6*m* LiBr at 235 K (simulation).

The 17 measured evaporation energies are displayed in Fig. 6(a) as multipliers of $2RT_{liq}$. They decline steadily with jet temperature from values of 1.7 near 235 K to 1.3 near 260 K. As in Fig. 5, we see no evidence for distinct behaviors of Cl^- and Br^-. Panel (b) compares these experimental measurements (solid symbols) with molecular dynamics simulations for pure water (open squares) and 4.0*m* and 8.6*m* LiBr (open circles).

TABLE II. Average kinetic energies of evaporating He atoms.

	Solution	T_{liq} (K)	$\langle E_{evap}\rangle$ in kJ mol^{-1} ($\langle E_{evap}\rangle/2RT_{liq}$)	No. of trials
Experiments[a]	Water	252	5.52 ± 0.25 (1.32 ± 0.06)	4
	4*m* LiCl	252	5.54 ± 0.42 (1.32 ± 0.10)	1
	8*m* LiCl	232	6.33 ± 0.27[b] (1.64 ± 0.07)	5
	8*m* LiCl	248	6.12 ± 0.41[b] (1.48 ± 0.10)	1
	4*m* LiBr	246	5.69 ± 0.41 (1.39 ± 0.10)	1
	8*m* LiBr	237	6.32 ± 0.28[b] (1.60 ± 0.07)	3
	8*m* LiBr	259	5.50 ± 0.43 (1.28 ± 0.10)	1
	8.5*m* LiBr	235	6.67 ± 0.31[b] (1.70 ± 0.08)	3
Simulations[c]	Water	235	4.83 ± 0.09 (1.24 ± 0.02)	
	Water	255	5.01 ± 0.09 (1.18 ± 0.02)	
	Water	298	5.63 ± 0.10 (1.14 ± 0.02)	
	4*m* LiBr	235	5.64 ± 0.09 (1.44 ± 0.02)	
	8.6*m* LiBr	235	6.02 ± 0.10 (1.54 ± 0.03)	
	8.6*m* LiBr	250	5.98 ± 0.09 (1.44 ± 0.02)	
	8.6*m* LiBr	260	6.09 ± 0.09 (1.41 ± 0.02)	

[a]Experimental uncertainties were estimated using a single 90% confidence interval derived from the 15 repeated measurements, a fitting uncertainty of $0.01 \times 2RT_{liq}$, and a temperature uncertainty of ±3 K.

[b]He evaporation monitored in the cylinder region. All other measurements recorded in the droplet region.

[c]Simulation uncertainties are 90% confidence intervals. All reported energies pertain to He evaporation in the droplet region.

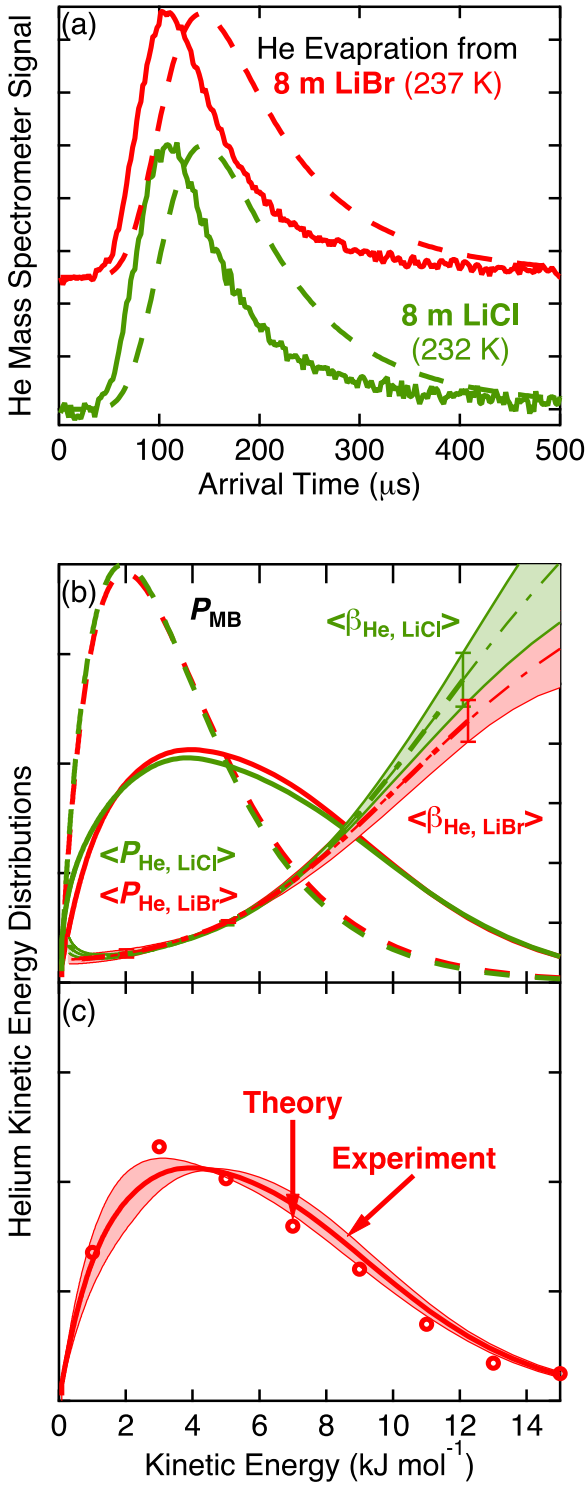

FIG. 5. (a) Helium evaporation from 8*m* LiBr (red) and LiCl (green) solutions. The dashed lines are MB distributions at 237 and 232 K. (b) Kinetic energy distributions P_{He} for LiCl (solid green) and LiBr (solid red) and P_{MB} (dashed green and red). The dashed-dotted green and red lines are the relative evaporation probabilities $\langle\beta_{He}(E)\rangle$. (c) Simulated and experimental $\langle P(E)\rangle$ distributions for 8.6*m* LiBr at 235 K.

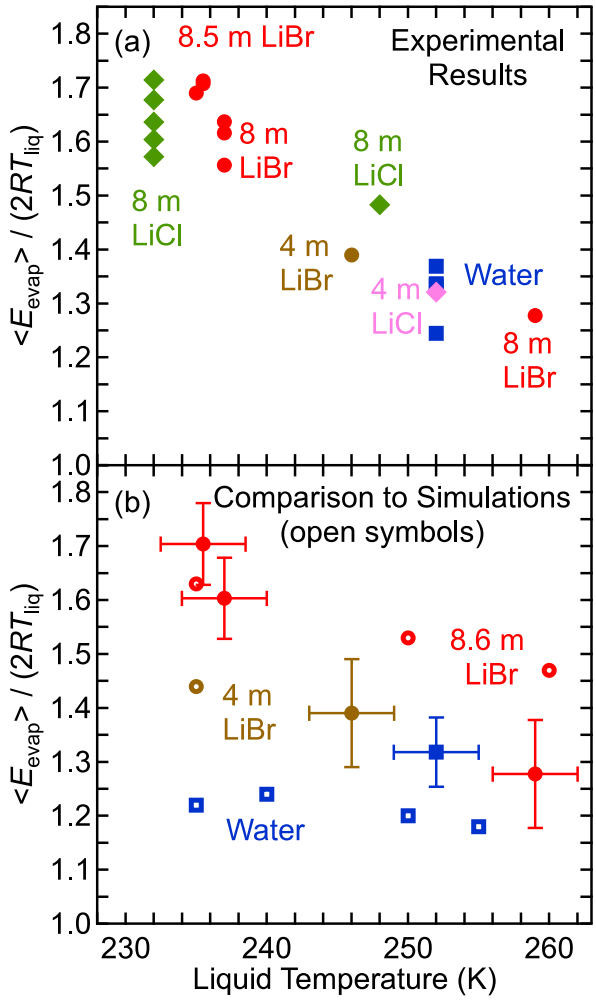

FIG. 6. (a) Helium kinetic energy in units of $2RT_{liq}$ versus liquid temperature determined from fits to argon evaporation. Each symbol represents one independent measurement. Pure water values are blue squares, 8*m* LiCl are dark green diamonds, 4*m* LiCl is a pink diamond, 8/8.5*m* LiBr are red circles, and 4*m* LiBr is a brown circle. (b) Comparison of simulated (open symbols) and experimental (filled symbols) values of $\langle E_{evap}\rangle$ for helium evaporation from pure water and LiBr solutions. Error bars are listed in Table II.

While the agreement is not exact, the simulated multipliers also generally fall with increasing temperature. The simulation values divide into two branches for pure water and the LiBr solution, separated by the intermediate experimental measurements. We show later that these multipliers partially merge when plotted against the He free energy of solvation. Both experimental and theoretical He evaporation energies are collected in Table II as energies and multipliers of $2RT_{liq}$.

V. ANALYSIS OF INDIVIDUAL AND AGGREGATE TRAJECTORIES

The simulations provide key insights into the location and timing of He atom acceleration and the forces that expel the atoms into the gas phase. Figure 7 illustrates two broad classes of trajectories for pure water at 255 K: He atoms that evaporate directly or "ballistically" (blue curves), representing the majority of the events, and He atoms that undergo one or more bounces before fully exiting the interfacial region (red curves). In panel (a), the dashed line represents the Gibbs dividing surface (GDS). The crossings in the single bounce trajectory are separated by 3 ps, consistent with the hovering trajectories identified in Ref. 19 for He evaporation from dodecane. Panel (b) reveals that He atoms rapidly accelerate

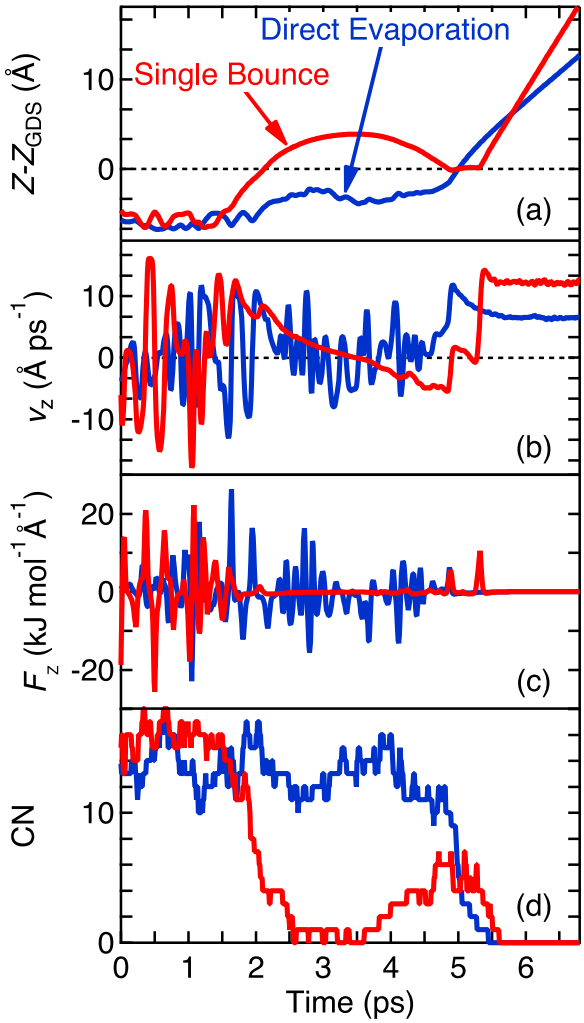

FIG. 7. Panels (a)–(d) show two classes of trajectories for He evaporating from pure water at 252 K. Direct evaporation (blue) is more common than multiple bounces (red). (a) Position of He atom perpendicular to the Gibbs dividing surface, (b) velocity v_z perpendicular to the surface, (c) normal force F_z acting on the He atoms, and (d) coordination number (CN) of water molecules around the He atom within the first solvation shell.

and decelerate in solution as they collide with solvent water molecules. Perhaps most important is the small deceleration of the He atom just before reaching a steady gas-phase velocity after 5–5.5 ps. This small reduction in speed reflects the weak He–water attractions that pull back slightly on the exiting He atoms. Panel (c) provides a view of the forces acting on the He atoms throughout the liquid. In particular, the last blue and red blips represent the forces on the He atoms as they are finally expelled from the surface; these forces are not larger than those constantly acting on the He atoms within the bulk water. The sharp reduction in these forces at 5–5.5 ps is accompanied by a sudden drop in the number of first-shell water molecules surrounding the He atom in panel (d) as He enters the gas phase. We identify a water molecule to be in the first-shell of a He atom if the O–He distance is less than the first minimum in the O–He radial distribution function, about 0.48 nm. This coordination number rises momentarily to half its value for the single bounce trajectory before the water molecules "kick" the He atom away.

The aggregate trajectories further reveal that, on average, the He atoms are accelerated in the interfacial region, where the density of water molecules declines rapidly. This is shown in Fig. 8(a), which displays the helium kinetic energy and density profile for pure water at 255 K averaged over 5000 He evaporation trajectories. The average kinetic energy first rises rapidly in the interfacial region by 1.4 kJ mol^{-1}. It then dips slightly by 0.3 kJ mol^{-1} as the He atoms move away from surface water molecules and decelerate as they escape the weak He–water attractive well. To categorize the nature of the collisions that lead to the overall acceleration of the He atoms, we plot the distribution of final turning-point collisions in blue. This distribution represents the position of the last collision in which a He atom turns around before escaping; the z-component of the velocity points inward toward the liquid before the collision and outward afterward. The turning points peak on the liquid phase side of the interface at −4 Å, accompanied by a smaller number of turning points around +2 to +4 Å. Most He atoms, therefore, undergo a final harsh collision within one monolayer of the Gibbs dividing surface

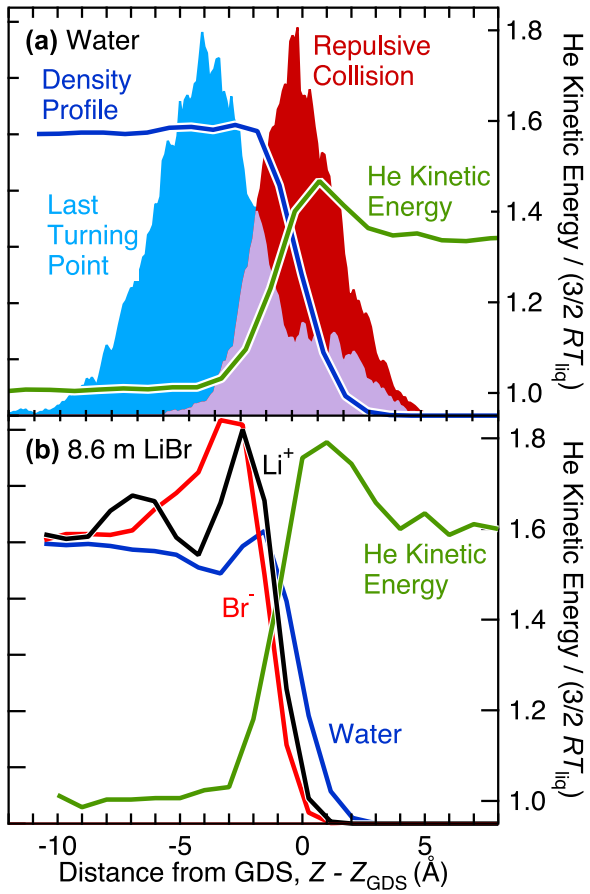

FIG. 8. (a) Density profile of water (blue line) and He kinetic energy (green line) overlaid with the distribution of last turning points (solid blue) and last repulsive interaction with water (solid red). (b) Density profiles of water (blue), bromide (red), and lithium (black) with average helium kinetic energy (green) for 8.6m LiBr at 250 K. The abscissa is the distance in Angstroms from the Gibbs dividing surface (GDS). Ion and water densities are normalized to the same value in the bulk, where the actual water/Li^+/Br^- ratio is 6.5/1/1. The He kinetic energy is determined by averaging over all He atoms in a thin slab at distance z and is therefore a density average, characterized by $\langle E_{MB} \rangle = 3/2RT_{liq}$ rather than $2RT_{liq}$.

on the liquid side; these He atoms must either pass through roughly one layer of water molecules or may launch from the surface in a depression or "valley" one layer deep. This turning point region does not overlap with the sharp increase in kinetic energy in green, suggesting that it is too strict a criterion for the final water-He collisions that accelerate the He atoms.

We then investigated another criterion, shown in red in Fig. 8(a), which overlaps well with the abrupt rise in average kinetic energy: this region represents the last repulsive collision between the He atom and a water molecule, and in most cases occurs after the last turning-point collision. We classify a repulsive collision as one that occurs at a distance smaller than the Lennard-Jones σ parameter, but with no restrictions on the angle of deflection. Together, the convergence of the drop in water density, increase in He kinetic energy, and peak in repulsive He–water collisions suggest that the He atom energy increases within the outermost 1–2 water layers from Maxwellian to super-Maxwellian by a repulsive collision between He and at least one water molecule. This picture is observed in numerous movies of the trajectories as well.

Figure 8(b) displays the relative density profiles for Li^+, Br^-, and H_2O for 8.6*m* LiBr at 235 K, along with the He kinetic energy distribution. In accord with previous simulations,[68] Li^+ is found to reside closer on average to the interface than Br^-, but both ion densities drop faster than the H_2O profile. Snapshots of the surface indicate that the ions lie primarily in valleys and are exposed to the vacuum. In the presence of these ions, the He kinetic energy rises in the interfacial region even more sharply (by 2.5 kJ mol^{-1}) than in pure water (1.4 kJ mol^{-1}), before dropping by 0.6 kJ mol^{-1} as it leaves the weak He-surface well. To quantify the forces acting on the He atom that generate this jump in kinetic energy, we next compute the He potential of mean force in the interfacial region.

VI. CORRELATIONS BETWEEN THE HE EVAPORATION ENERGY AND POTENTIAL OF MEAN FORCE

At thermal equilibrium, the average force acting on a solute atom in the interfacial region is equal to the negative derivative of the PMF in this region. This average force rigorously applies to solute atoms that evaporate slowly enough to sample all solvent configurations as they traverse the interfacial region. In this case, the solute atoms collide extensively with solvent molecules and possess a MB distribution of speeds, emerging with an average flux-weighted energy of $2RT_{liq}$. The forces acting on evaporating He atoms, however, will not necessarily be derivable from the PMF because these weakly interacting atoms may spend too little time near the surface to sample the full distribution of water configurations. Indeed, the super-Maxwellian He kinetic energies we observe imply that this equilibration cannot prevail throughout the entire interfacial region. The calculated PMFs, while not yielding the exact forces on the He atoms, still provide insights into these forces and even afford predictions of the He evaporation energies for other temperatures and solvents. This analysis is presented below.

The computed PMFs for He in pure water at 235 and 255 K and in 8.6*m* LiBr at 250 K are plotted in Fig. 9(a). The asymptotic difference between the liquid and gas states is simply the equilibrium free energy of solvation ΔG^{o}_{solv} of He in each solution.[2] (Free energies extracted from the PMF asymptotes differ slightly from those in Fig. 2 because finite size effects were not taken into account in the more time-intensive PMF calculations.) In particular, the (positive) free energy difference is highest for 8.6*m* LiBr at 250 K and lowest for pure water at 235 K. Unlike PMFs for the transport of more soluble gases across the water-vapor interface,[2,69–73] the helium PMFs decrease sharply from liquid to vapor with no discernable minima near the surface. These steep downward slopes imply that interfacial water molecules repel the He atoms away from solution and accelerate them through the interfacial region; this repulsive force is generated by relaxation of the local water structure that has been perturbed by the interloping He atom.[74]

We focus on pure water at 255 K and plot the PMF and the negative of its derivative along the *z*-direction in Fig. 9(b). This derivative is the average force acting on a He atom normal to the surface as the He atom samples all solvent configurations and is ejected into vacuum. It overlaps closely with the drop in density and rise in the kinetic energy (plotted in Fig. 8(a)). The consequences of this repulsive mean force can be viewed in two extreme limits. Solutes that interact strongly with the solvent will undergo energy-exchanging collisions throughout the interfacial region and will exit at

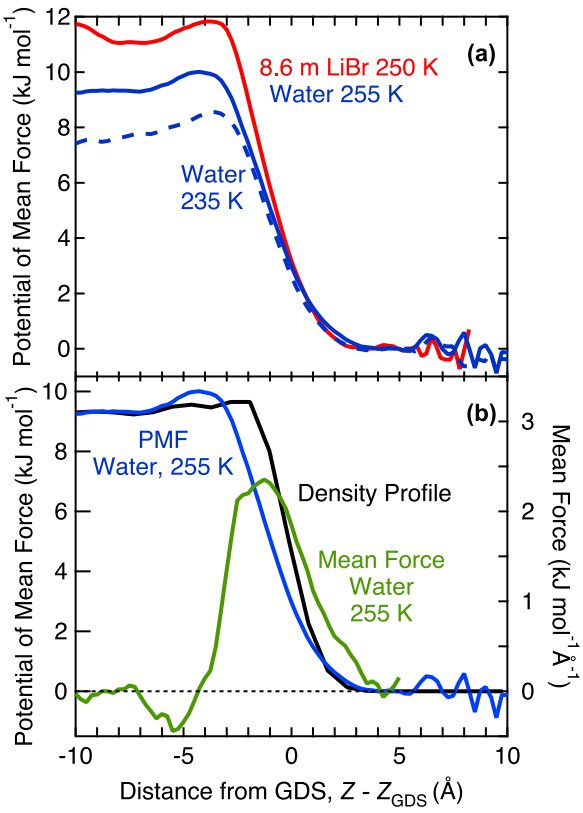

FIG. 9. (a) Potentials of mean force (PMF) for He in pure water (235 and 255 K) and 8.6*m* LiBr/H_2O at 250 K. (b) Density profile (black), PMF (blue) and mean force (green) acting on a He atom in pure water at 255 K.

energies with a flux-weighted z-component equal to RT_{liq}. These solutes are accelerated by repulsive forces generated by the relaxing water structure, but the excess energy is efficiently dissipated into the surrounding water molecules. It is likely that nearly all solutes (except for He, Ne, and H_2) fall within or close to this full dissipation regime. In the opposite extreme, a hypothetical solute with vanishingly small solute-water interactions will exit with a z-component of the kinetic energy increased by the entire positive free energy of solvation with respect to the gas phase. In this case, no gas-water collisions will occur to remove the excess energy imparted by the instantaneous rearrangement of the water structure.

Helium falls within these two extremes: He atoms evaporate from pure water at 255 K with a computed z-component of the flux-weighted kinetic energy of 3.2 kJ mol^{-1}, which exceeds the value of RT_{liq} = 2.1 kJ mol^{-1}. Although the excess energy is small in comparison to ΔG^{o}_{solv} = 8.6 kJ mol^{-1}, it may nevertheless represent the maximum observable deviation among all solute species because He atoms possess the smallest polarizability and the weakest solute-solvent attractions. As shown in Figs. 8(a) and 9(b), the forces that give rise to this acceleration and detachment from thermal equilibrium begin about −4 Å from the GDS and extend to +3 Å as the density decreases and the He atoms cease to dissipate their excess energy through He–water collisions.

A fascinating implication of Fig. 9 is that higher free energies of solvation may generate greater averaged forces on the exiting He atom and therefore eject the atom at higher kinetic energies. In order to explore this conjecture, we combined the calculated free energies in Fig. 2 with the simulated and measured kinetic energies in Table II to construct Fig. 10(a). This panel naturally separates into regions of pure and salty water because of the lower solubility (and higher free energy) of He atoms in the presence of the Li^+ and Br^- ions in solution. Panel (a) reveals that the total kinetic energies do rise with ΔG^{o}_{solv}, in part reflecting increasingly steep potentials of mean force in the interfacial region. Helium evaporation from two other liquids, dodecane and ethylene glycol at 295 K,[18] also fits the trend observed for pure and salty water, suggesting a general link between the He atom evaporation and solvation free energies.

The total He kinetic energies in Figure 10(a) may be viewed as a sum of the flux-weighted Maxwellian energy of $2RT_{liq}$ and an excess kinetic energy. To isolate this non-Maxwellian component, we plot $\langle E_{evap}\rangle - 2RT_{liq}$ against ΔG^{o}_{solv} in panel (b). This panel further suggests that the excess kinetic energy itself increases with the free energy of solvation, although the points are significantly more distributed than in panel (a). In particular, the excess values appear to decrease with temperature within the cluster of points for water (at lower ΔG^{o}_{solv}) and for 8-8.6m LiBr (at higher ΔG^{o}_{solv}). This trend may reflect changes in interfacial roughness and in the nature of He–water collisional energy transfer at higher temperature. We hope to investigate these effects in future studies and clarify the correlation between $\langle E_{evap}\rangle - 2RT_{liq}$ and ΔG^{o}_{solv} by surveying solutions encompassing even broader ranges in temperature and ion concentration.

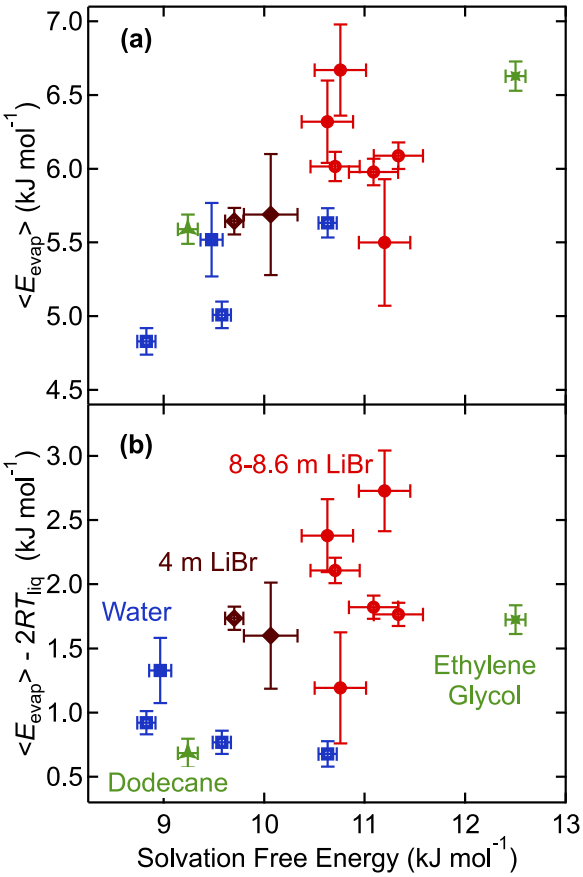

FIG. 10. (a) Helium evaporation energy versus calculated He free energy of solvation, ΔG^{o}_{solv}, and (b) He excess kinetic energy, $\langle E_{evap}\rangle - 2RT_{liq}$, for the same points in panel (a). Open symbols represent simulations and closed symbols represent measurements for water (blue squares), 4m LiBr (brown diamonds), and 8-8.6m LiBr (red circles). Data for dodecane and ethylene glycol are added in green. Values of ΔG^{o}_{solv} for 4 and 8m LiBr are linearly interpolated from the 0 and 8.6m LiBr simulations.

VII. CONCLUDING REMARKS

The experiments in this work and two previous studies[17,18] demonstrate that He atoms evaporate in super-Maxwellian distributions from liquids spanning pure and salty water, alkanes, aromatics, and alcohols. A statistical mechanical interpretation of these measurements presented here reveals a promising link between the kinetic energies of the evaporating He atoms and the potentials of mean force acting on the He atoms in the interfacial region. Figure 10(a) summarizes this correlation by showing that the average He kinetic energy tracks the free energy of solvation. In this picture, $\Delta G^{o}_{solv} = -RT \ \ln(n(\mathrm{He})_{water}/n(\mathrm{He})_{gas})$ is the free energy difference between He dissolved in solution and He in the gas phase and represents the integrated force on the He atom as it is ejected into vacuum. Larger solvation free energies imply greater forces and acceleration of the He atoms in the interfacial region. Some of this extra translational energy is not dissipated within the solvent because of insufficient He-solvent collisions in the outermost surface region. This incomplete thermalization leaves the He atoms with an excess kinetic energy that roughly correlates with the free energy difference (Figure 10(b)). An essential aspect of this picture is the focus on potentials of mean force rather than on

He–water potential energies, as the PMFs naturally average over all configurations of the water molecules. An even more precise picture likely lies between these descriptions, one that explicitly incorporates the time scales of He and water motions and the kinematics of interfacial He–water and He-ion collisions.

ACKNOWLEDGMENTS

This research was funded by NSF No. CHE-1152737 for C.H., J.F., and G.N. and by NSF No. CHE-1058752 and the University of Wisconsin Foundation for Z.K. and J.S. J.F. received additional funding from NSF No. DGE-0718123. We thank Ilan Benjamin, Sven Koehler, Bruce Kay, and Dor Ben-Amotz for many enlightening discussions.

[1]L. L. Loeb, *The Kinetic Theory of Gases* (McGraw-Hill, New York, 1927).
[2]B. C. Garrett, G. K. Schenter, and A. Morita, Chem. Rev. **106**, 1355 (2006).
[3]C. T. Rettner, E. K. Schweizer, and C. B. Mullins, J. Chem. Phys. **90**, 3800 (1989).
[4]K. W. Kolasinski, *Surface Science: Foundations of Catalysis and Nanoscience*, 3rd ed. (Wiley, United Kingdom, 2012).
[5]L. P. Dempsey, S. M. Brastad, and G. M. Nathanson, J. Phys. Chem. Lett. **2**, 622 (2011).
[6]J. E. Hurst, L. Wharton, K. C. Janda, and D. J. Auerbach, J. Chem. Phys. **83**, 1376 (1985).
[7]M. E. Saecker and G. M. Nathanson, J. Chem. Phys. **99**, 7056 (1993).
[8]M. J. Cardillo, M. Balooch, and R. E. Stickney, Surf. Sci. **50**, 263 (1975).
[9]J. C. Tully, Surf. Sci. **111**, 461 (1981).
[10]G. Comsa and R. David, Surf. Sci. Rep. **5**, 145 (1985).
[11]M. J. Weida, J. M. Sperhac, and D. J. Nesbitt, J. Chem. Phys. **105**, 749 (1996).
[12]H. A. Michelsen, C. T. Rettner, D. J. Auerbach, and R. N. Zare, J. Chem. Phys. **98**, 8294 (1993).
[13]A. Hodgson, Prog. Surf. Sci. **63**, 1 (2000).
[14]T. Matsushima, Surf. Sci. Rep. **52**, 1 (2003).
[15]M. Faubel, S. Schlemmer, and J. P. Toennies, Z. Phys. D **10**, 269 (1988).
[16]M. Faubel and T. Kisters, Nature **339**, 527 (1989).
[17]A. M. Johnson, D. K. Lancaster, J. A. Faust, C. Hahn, A. Reznickova, and G. M. Nathanson, J. Phys. Chem. Lett. **5**, 3914 (2014).
[18]D. K. Lancaster, A. M. Johnson, K. Kappes, and G. M. Nathanson, J. Phys. Chem. C **119**, 14613 (2015).
[19]S. V. P. Koehler and M. A. Williams, Chem. Phys. Lett. **629**, 53 (2015).
[20]I. Benjamin, personal communication, 2013.
[21]L. F. Phillips, Chem. Phys. Lett. **458**, 388 (2008).
[22]D. Lancaster, Ph.D. thesis, University of Wisconsin-Madison, 2014.
[23]J. R. Morris, P. Behr, M. D. Antman, B. R. Ringeisen, J. Splan, and G. M. Nathanson, J. Phys. Chem. A **104**, 6738 (2000).
[24]S.-C. Park, D. K. Burden, and G. M. Nathanson, J. Phys. Chem. A **111**, 2921 (2007).
[25]T. Somasundaram and R. M. Lynden-Bell, Mol. Phys. **97**, 1029 (1999).
[26]P. Varilly and D. Chandler, J. Phys. Chem. B **117**, 1419 (2013).
[27]Z. R. Kann and J. L. Skinner, "Sub- and super-Maxwellian evaporation of simple gases from liquid water" (unpublished).
[28]For studies of rotational vibrational relaxation throughout the evaporation process, see O. J. Maselli, J. R. Gascooke, W. D. Lawrance, and M. A. Buntine, Chem. Phys. Lett. **513**, 1 (2011).
[29]M. Faubel, in *Photoionization and Photodetachment: Part I*, edited by C.-Y. Ng (World Scientific, Singapore, 2000).
[30]A. H. Lefebvre, *Atomization and Sprays* (Hemisphere Publishing, New York, 1989).
[31]W. G. Hoover, Phys. Rev. A **31**, 1695 (1985).
[32]H. J. C. Berendsen, D. van der Spoel, and R. van Drunen, Comput. Phys. Commun. **91**, 43 (1995).
[33]E. Lindahl, B. Hess, and D. van der Spoel, J. Mol. Model. **7**, 306 (2001).
[34]C. J. Tainter, P. A. Pieniazek, Y.-S. Lin, and J. L. Skinner, J. Chem. Phys. **134**, 184501 (2011).
[35]J. L. F. Abascal and C. Vega, J. Chem. Phys. **123**, 234505 (2005).
[36]Z. R. Kann and J. L. Skinner, J. Chem. Phys. **141**, 104507 (2014).
[37]A. H. Mao and R. V. Pappu, J. Chem. Phys. **137**, 064104 (2012).
[38]R. W. Bickes, Jr., G. Duquette, C. J. N. van den Meijdenberg, A. M. Rulis, G. Scoles, and K. M. Smith, J. Phys. B **8**, 3034 (1975).
[39]A very recent study provides an alternative set of Lennard-Jones parameters for He-O interactions, see O. Warr, C. J. Ballentine, J. Mu, and A. Masters, J. Phys. Chem. C **119**, 14486 (2015).
[40]For studies of He diffusion in amorphous ice that probe nonspherical He–water interactions, see J. L. Daschbach, G. K. Schenter, P. Ayotte, R. S. Smith, and B. D. Kay, Phys. Rev. Lett. **92**, 198306-1–198306-4 (2004).
[41]D. Berthelot, C. R. Acad. Sci. **126**, 1703 (1898).
[42]H. A. Lorentz, Ann. Phys. **248**, 127 (1881).
[43]M. P. Allen and D. J. Tildesley, *Computer Simulation of Liquids* (Oxford, New York, 1989).
[44]J. S. Hub, B.L.de. Groot, and D. van der Spoel, J. Chem. Theory Comput. **6**, 3713 (2010).
[45]C. H. Bennett, J. Comput. Phys. **22**, 245 (1976).
[46]M. Parrinello and A. Rahman, J. Appl. Phys. **52**, 7182 (1981).
[47]L. Greenspan, J. Res. Natl. Bur. Stand., Sect. A **81A**, 89 (1977).
[48]P. E. Mason, S. Ansell, G. W. Neilson, and S. B. Rempe, J. Phys. Chem. B **119**, 2003 (2015).
[49]V. Migliorati, F. Sessa, G. Aquilanti, and P. D'Angelo, J. Chem. Phys. **141**, 044509 (2014).
[50]K. Ibuki and P. A. Bopp, J. Mol. Liq. **147**, 56 (2009).
[51]Y. Marcus, J. Solution Chem. **38**, 513 (2009).
[52]S. Bouazizi and S. Nasr, J. Mol. Struct. **875**, 121 (2008).
[53]W. Yao, H. Bjurström, and F. Setterwall, J. Chem. Eng. Data **36**, 96 (1991).
[54]M. R. Conde, Int. J. Therm. Sci. **43**, 367 (2004).
[55]I. Sawada, M. Yamada, S. Fukusako, and T. Kawanami, Int. J. Thermophys. **19**, 749 (1998).
[56]V. P. Mashovet, N. M. Baron, and M. U. Shcherba, Zh. Prikl. Khem. **44**, 1981 (1971).
[57]A. Dehaoui, B. Issenmann, and F. Caupin, Proc. Natl. Acad. Sci. U. S. A. **112**, 12020 (2015).
[58]H. L. Clever, *Helium and Neon (vol. 1) and Oxygen and Ozone (vol. 7)*, IUPAC Solubility Data Series (Pergamon, New York, 1979).
[59]This free energy corresponds to the ρ-process in the designations provided on page 204, A. Ben-Naim, *Molecular Theory of Solutions* (Oxford, Great Britain, 2006).
[60]Helium, neon, and oxygen solubilities in salt solutions are reviewed in Ref. 58 on pp. 20 and 142 (Vol. 1) and on pp. 67–69 (Vol. 7). There is no data for He in LiBr. We instead compare LiCl, NaCl, and NaBr. The He solubility ratios at 1m salt are LiCl/NaCl/NaBr/water = 0.86/0.80/0.79/1. The analogous Ne solubilities are LiCl/NaCl/NaBr/water = 0.83/0.77/0.77/1. The gas closest to He for which LiBr solubility exists is O_2, with the following values: LiCl/LiBr/NaCl/NaBr/water = 0.85/0.82/0.72/0.74/1. In all cases, the differences between the chloride and bromide salts are very small.
[61]F. A. Long and W. F. McDevit, Chem. Rev. **51**, 119 (1952).
[62]W. A. Gerth, J. Solution Chem. **12**, 655 (1983).
[63]L. Li, C. J. Fennell, and K. A. Dill, J. Chem. Phys. **141**, 22D518 (2014).
[64]J. S. Becker, R. D. Brown, E. Johansson, N. S. Lewis, and S. J. Sibener, J. Chem. Phys. **133**, 104705 (2010).
[65]V. Sadtchenko, M. Brindza, M. Chonde, B. Palmore, and R. Eom, J. Chem. Phys. **121**, 11980 (2004).
[66]J. D. Smith, C. D. Cappa, W. S. Drisdell, R. C. Cohen, and R. J. Saykally, J. Am. Chem. Soc. **128**, 12892 (2006).
[67]D. J. Auerbach, in *in Atomic and Molecular Beam Methods*, edited by G. Scoles (Oxford, New York, 1988).
[68]F. Bresme, E. Chacon, P. Tarzona, and A. Wynveen, J. Chem. Phys. **137**, 114706 (2012).
[69]T. Somasundaram, R. M. Lynden-Bell, and C. H. Patterson, Phys. Chem. Chem. Phys. **1**, 143 (1999).
[70]T. Somasundaram, M. in het Panhuis, R. M. Lynden-Bell, and C. H. Patterson, J. Chem. Phys. **111**, 2190 (1999).
[71]R. S. Taylor and B. C. Garrett, J. Phys. Chem. B **103**, 844 (1999).
[72]L. M. Dang and B. C. Garrett, Chem. Phys. Lett. **358**, 309 (2004).
[73]J. Vieceli, M. Roeselová, N. Potter, L. M. Dang, B. C. Garrett, and D. J. Tobias, J. Phys. Chem. B **109**, 15876 (2005).
[74]D. Chandler, Nature **437**, 640 (2005).
[75]J. Pátek and J. Klomfar, Int. J. Refrig. **29**, 566 (2006).
[76]D. M. Murphy and T. Koop, Q. J. R. Meteorol. Soc. **131**, 1539 (2005).
[77]K. R. Patil, A. D. Tripathi, G. Pathak, and S. S. Katti, J. Chem. Eng. Data **35**, 166 (1990).